

D.R. Mason, A.E. Sand, X. Yi, S.L. Dudarev

Direct observation of the spatial distribution of primary cascade damage in tungsten

Enquiries about copyright and reproduction should in the first instance be addressed to the Culham Publications Officer, Culham Centre for Fusion Energy (CCFE), Library, Culham Science Centre, Abingdon, Oxfordshire, OX14 3DB, UK. The United Kingdom Atomic Energy Authority is the copyright holder.

Direct observation of the spatial distribution of primary cascade damage in tungsten

D.R. Mason ^a, A.E. Sand ^{a,b}, X. Yi ^c, S.L. Dudarev ^a

^a *CCFE, UK Atomic Energy Authority, Culham Science Centre, Abingdon, Oxfordshire
OX14 3DB, United Kingdom*

^b *Department of Physics, University of Helsinki, P.O. Box 43, FI-00014, Helsinki, Finland*

^c *School of Materials Science and Engineering, University of Science and Technology
Beijing, 100083, Beijing, China*

Direct observation of the spatial distribution of primary cascade damage in tungsten

D.R. Mason^{a,*}, A.E. Sand^{a,b}, X. Yi^c, S.L. Dudarev^a

^a*CCFE, UK Atomic Energy Authority, Culham Science Centre, Abingdon, Oxfordshire OX14 3DB, United Kingdom*

^b*Department of Physics, University of Helsinki, P.O. Box 43, FI-00014, Helsinki, Finland*

^c*School of Materials Science and Engineering, University of Science and Technology Beijing, 100083, Beijing, China*

Abstract

Recently we have presented direct experimental evidence for large defect clusters being formed in primary damage cascades in self-ion irradiated tungsten [Yi et al, EPL 110:36001 (2015)]. This large size is significant, as it implies strong elastic interaction between the defects will affect their subsequent evolution, especially if defects are formed close together. In this work we propose and validate a simple exponential form for the spatial distribution of defects within a single cascade. The cascade statistics necessary have been acquired by developing an automated procedure for analyzing black-dot damage on transmission electron microscope micrographs. We confirm that the same model also produces a high-quality fit to the separation between larger defects observed in MD simulations. For the first time we present experimental evidence for the sub-nanometre-scale spatial distribution of defect clusters within individual cascades.

Keywords: irradiation damage, electron microscopy, defect clusters, spatial correlation

1. Introduction

Microstructural evolution of tungsten under irradiation has attracted significant attention since tungsten has been chosen as a plasma facing material for ITER [1]. Tungsten is a brittle metal, particularly prone to brittle failure at grain boundaries, and its thermomechanical properties only worsen on exposure to irradiation [2, 3, 4]. Understanding engineering properties is an inherently multiscale challenge, from the electrons in the bonds between atoms to the movement of dislocations, so it is essential that high-quality information is passed from one scale to the next[5]. As each primary damage cascade is different, whether initiated by a high energy neutron in a reactor or by a high energy ion in the lab, this information must have a solid statistical underpinning: rare events which may dominate microstructural evolution are unlikely to be captured in a small molecular dynamics (MD) database.

*Corresponding author

Email address: `daniel.mason@ukaea.uk` (D.R. Mason)

Previously we have observed the average number of defect clusters formed directly in collision cascades, and containing n point defects, is well represented by a power-law $f(n) \sim A/n^S$, both in MD[6, 7] and experiment[8], and accounted for the deviation from power-law behaviour at large sizes[9]. An important point noted in these papers is that large defect clusters are statistically significant, and we have shown that large interstitial loops interact strongly via their elastic fields[10]. We have not previously been able to find a good model for exactly how closely together defects are produced. This paper addresses this spatial separation problem directly, by analyzing images of ultra-high-purity tungsten foils irradiated with tungsten self-ions in a cryogenic *in situ* transmission electron microscope (TEM).

To enable the fitting of spatial distribution functions, our model for the production of defects visible in the TEM is highly idealized and simplified. This is necessary as a state-of-the-art object Kinetic Monte Carlo model[11, 12] would require thousands of independent simulation runs to judge the quality of each trial fit[10]. We assume that the visible defects are $1/2\langle 111 \rangle$ interstitial-type loops[13, 10, 8]. We further assume these defects are mobile- even at 30K- and move in one-dimension on their glide cylinders. As skew cylinders rarely intersect, there is no appreciable growth of clusters after generation[9]. Vacancy motion and self-climb will be inactive at this temperature[14]. The defect clusters may in reality be pinned by vacancy clusters, impurity atoms, or other sessile atomic configurations; we simplify by stating that a one-dimensional migrating loop is unlikely to hit a pinning site in our ultra-high-purity foil sample[10]. Loop retention is therefore considered to be solely a result of mutual elastic trapping of loops on skew glide cylinders[15, 10, 9]

We show that the probability of a defect cluster produced a distance r from the centre of a cascade is given by $p(r) \sim \exp(-r/\lambda)$. We find that there is some evidence, from comparison of MD simulation results to electron microscope images of cascade defects, that larger loops may be produced closer to the centre of the cascade, but are unable to quantify this effect.

In section 2 we describe MD simulations and *in situ* TEM experiments and generate pair radial distribution functions for the observed distance between pairs of defects. To generate statistics for the spatial separation between defects produced in single cascades, we have analysed many thousands of spots on micrographs. To do this reliably and reproducibly, we have automated the analysis of micrographs. In section 3 we outline the mathematical formalism for parameterizing a functional form for the generation of defects, which reproduces these radial distribution functions. Finally in section 4 we compare the spatial generation of defects as found in MD and experiment, and comment on the significance for subsequent microstructural evolution.

2. Generating radial distribution functions with *in situ* TEM and MD

2.1. TEM

In situ irradiations were performed at the IVEM-Tandem Facility at Argonne National Laboratory. 3mm discs were cut from tungsten sheets (Plansee Ultra-High Purity-W (UHP-W), > 99.996 wt% pure), heat-treated in vacuum at 1673

K for 20 hours, and finally twin-jet electropolished with 0.5wt% NaOH aqueous solution to reach TEM transparency thickness ($\lesssim 100\text{nm}$). The average grain size after treatment was $10\mu\text{m}$, and very few dislocations were observed to remain. The samples were cooled to 30K, and (001) grains were irradiated with tungsten ions, at an incidence angle 15° off normal. Ion energies were 50, 150, 300, 400keV up to $1.25 \times 10^{16}\text{W}^+/\text{m}^2$.

Each foil region was imaged in weak-beam dark-field conditions, using ($\mathbf{g} = 200, 4.25\text{g}$; $\mathbf{g} = 200, 4.75\text{g}$; $\mathbf{g} = 200, 5.25\text{g}$; $\mathbf{g} = 110, 5.25\text{g}$; $\mathbf{g} = 110, 7.25\text{g}$; and $\mathbf{g} = 110, 7.75\text{g}$). Regions were superimposed using the convergent weak beam technique of Prokhodtseva et al. [16], and then analysed with the technique described below. A summary of the areas studied and number of spots counted in each is given in table 2.

We automate the analysis of the micrographs with a new algorithm developed from the method described in ref [8]. The algorithm has two parts: first the background fluctuations are removed, then the features (which in this case are small bright spots) fitted to 2d Gaussian profiles. A brief description is given in appendix Appendix A; a full description and comparison to other techniques is beyond the scope of this article.

2.2. MD

Individual collision cascades from recoils in bulk, and from ions incident on a foil, were simulated with the classical molecular dynamics code PARCAS [17, 18, 19, 20]. The simulation method is detailed in [7], and specifics of the foil irradiation simulations are given in [8]. Briefly, cascades were initiated by giving an atom a kinetic energy of 150 keV in a random direction in bulk, and inclined 15° from the surface normal on foils. The simulation cells contained 6.8 million (bulk) or 10.9 million (foil) atoms. For bulk simulations, periodic boundaries were applied in all directions, while for foil simulations the borders in one direction were open, forming the top and bottom surfaces of the foil, with a thickness of 65 nm. The initial temperature of the cell was 0 K, and a Berendsen thermostat [21] set to 0 K was applied to the atoms in a 1.5 unit cell thick region along all periodic boundaries. The interatomic potential for tungsten by Derlet et al. [22] was used for all simulations. A non-local friction force was applied to all atoms with kinetic energy above 10 eV to account for energy losses due to electronic stopping. The stopping power was determined by the method used in SRIM [23]. Cascades were followed until cool, at which point the defects were stable, which amounted to 40 ps in bulk, and 60 ps in foils.

Final defects were analysed using the Wigner-Seitz cell method, which is space-filling, and labels empty cells as vacancies and multiply occupied cells as interstitials. Defects resulting from this analysis that were located at the surface of the foil, or due to rearrangement of surface atoms, were disregarded. Clusters were determined by an automated method, where two interstitials were considered as belonging to the same cluster if they lay within third nearest neighbour distance of each other. The choice of cut-off distance for the cluster analysis, within a few nearest neighbors, is found to have little effect on the results, as SIA clusters tend to be compact, and well separated from each other. The centre of position of a cluster is taken as the mean centre of position of all Wigner-Seitz cells associated with the cluster.

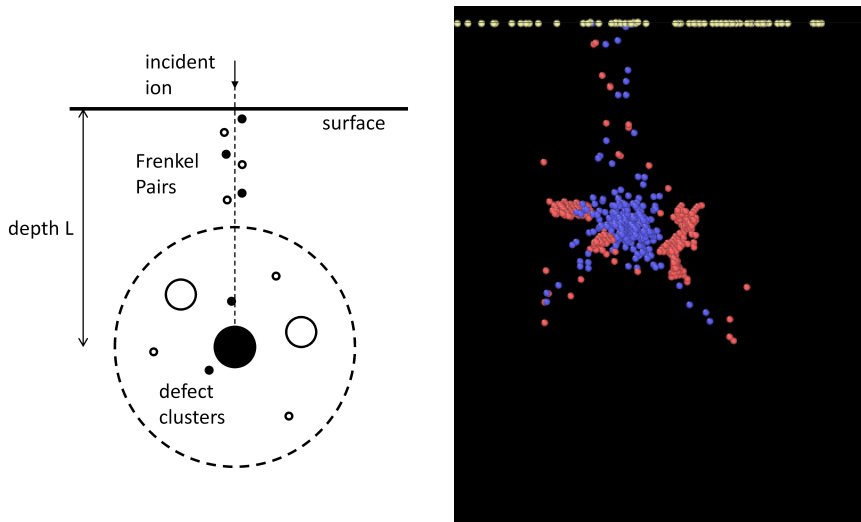


Figure 1: Left: A cartoon of a cascade initiated in a foil by a high energy self-ion. The incident ion may channel some distance through the foil, producing a handful of Frenkel pair defects along its path. At some depth L a heat spike is initiated, which after recrystallization leaves defect clusters in a range of sizes. We simplify by considering defect clusters to be either interstitial- type (open circles) or vacancy- type (filled circles). Right: An example MD simulation of a 150keV ion penetrating a foil, snapshot taken at 60 ps. Blue dots are vacancies, red are interstitials.

MD foil simulations typically proceed along the lines of the cartoon in figure 1. The incident ion may channel some distance through the crystal lattice, leaving some Frenkel pairs along its path. Then a heat spike is initiated at a depth L below the surface. After recrystallization defect clusters remain. In MD simulations, and so most likely in reality, these clusters can be extremely complex. We will simplify and categorize them as being either of interstitial- or vacancy- type, quasi-independent objects. In this work we consider only the interstitial defect clusters. In figure 1 there are $N = 8$ interstitial defect clusters shown, of which three are crowdions in the channelling path and two are larger. To find the spatial separation of defects within the cascade region, we should exclude these Frenkel pairs in the channelling path. To compare to experiment, we should find the spatial separation appropriate for the larger defect clusters, as only these would be visible in the TEM.

3. The spatial separation of defect clusters in primary damage cascades

In this section we propose an analytical functional form for the distribution of defects produced within a single irradiation damage cascade which we may compare to MD, and then go on to derive a form for the observed distribution in an *in situ* TEM experiment.

To start our analysis, we will look at the separation between two defects produced in the same cascade. A single high-energy displacement cascade can be thought of as a branching tree of subcascades[24, 25, 26]. A full analysis of

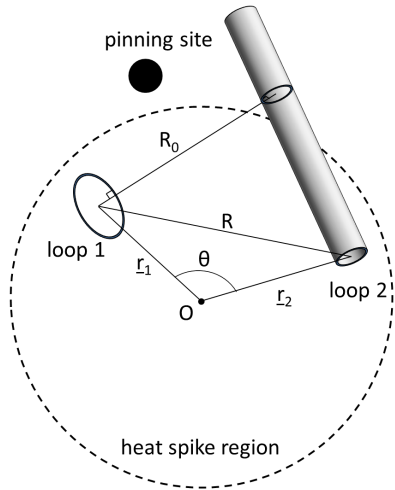


Figure 2: Sketch of our model for the geometry of cascades. Loops 1 and 2 are produced a vector separation \vec{r}_1 and \vec{r}_2 from the origin of the cascade; their initial separation is R . One loop then moves on its glide cylinder until it reaches a minimum separation R_0 . If the elastic interaction at separation R_0 is great enough, the loops are mutually trapped, otherwise they are lost to the surface. Note that 1d diffusing objects in 3d space are unlikely to collide with each other or with sufficiently dilute sessile pinning sites.

the cascade spatial structure should therefore have a rule for the production of defects within a single subcascade, a rule for the branching of a cascade into subcascades, and a rule for the separation of subcascades. We have found in this study that including rules for subcascade branching can improve the fit to the experimental data at the expense of additional parameters. The improvement is not *significant* in a chi-squared sense. This is most likely because we observe individual cascades amongst a background of independent cascades, which obscures any long-range spatial information. We can therefore continue by considering each cascade to be spherically symmetric. This is valid in the case of tungsten cascades, where the subcascade splitting threshold is high[27, 26]. For high-energy iron cascades it may be necessary to use a full formulation including the treatment of splitting of a cascade into subcascades (see section 3.1).

The geometry used for describing defect clusters spatial distribution is illustrated in figure 2. One defect cluster is generated at \vec{r}_1 with respect to its parent cascade origin, and the other generated at \vec{r}_2 . The probability that they are separated by distance R in 3-d space is

$$4\pi R^2 P_{3d}(R) \equiv \int \int p(\vec{r}_1, \vec{r}_2) \times \delta[|\vec{r}_1 - \vec{r}_2| - R] d^3\vec{r}_1 d^3\vec{r}_2, \quad (1)$$

where for convenience we *defined* the radial probability distribution in such a way that it is normalized as follows

$$\int P_{3d}(R) 4\pi R^2 dR = 1. \quad (2)$$

To simplify the six-dimensional integral in (1), we assume that the generating function within one cascade is both spherically symmetric and separable (ie the

positions of the generated defects are independent).

$$p(\vec{r}_1, \vec{r}_2) \equiv p(|\vec{r}_1|)p(|\vec{r}_2|), \quad (3)$$

with normalisation

$$\int p(r) 4\pi r^2 dr = 1. \quad (4)$$

We can perform the integral in equation 1 in spherical polars, with the angle between the two defects and origin θ , and exploit the azimuthal symmetry to write

$$4\pi R^2 P_{3d}(R) = \int p(r_1)p(r_2) \delta \left[\sqrt{r_1^2 + r_2^2 - 2r_1r_2 \cos \theta} - R \right] \\ \times 4\pi r_1^2 dr_1 4\pi r_2^2 dr_2 \frac{\sin(\theta)}{2} d\theta, \quad (5)$$

leaving the simple double-integral expression

$$P_{3d}(R) = \frac{2\pi}{R} \int_{r_1=0}^{\infty} \int_{r_2=|R-r_1|}^{R+r_1} p(r_1)p(r_2) r_1 r_2 dr_1 dr_2. \quad (6)$$

This expression is normalised according to (2). The radial distribution function is the expected number of defects separated by a distance in the range from R and $R + dR$:

$$g_{3d}(R)dR = N_{\text{pairs}} P_{3d}(R) 4\pi R^2 dR, \quad (7)$$

Equation 7 may be directly compared to a histogram generated from MD cascade simulations where N_{pairs} pairs of defects were counted (see figure 3).

We now move to consider the distribution of loops observed in an *in situ* TEM experiment. To compare to *in situ* TEM experiments we must work with the 2d projection of equation 6, and account for the background of defects produced in other cascades. The projection in 2d of a cascade produced at depth L is readily found in cylindrical polar coordinates:

$$P_{2d}(\rho) = \int_{z=-\infty}^L P_{3d}(R = \sqrt{\rho^2 + z^2}) dz, \quad (8)$$

which has normalisation $\int P_{2d}(\rho) 2\pi d\rho = 1$ as $L \rightarrow \infty$. But what is actually observed is somewhat more complex: we must develop this expression to account for overlapping spots, the proportion retained in the foil, and the background of independent cascades.

One of the most obvious differences between MD and experiment is the time scale. To compare simulations to experiment, we must always consider that the defects formed in cascades might be mobile. For *in situ* ion irradiation this has the added complication that defects may be lost to the foil surface unless they are trapped. Following Ref. [10], we assume that for ion irradiation of this ultra-high purity foil, mutual elastic trapping is solely responsible for the retention of loops in the foil. Mobile defects may move along their glide cylinders until they reach a position of elastic minimum energy, as shown in figure 2. We

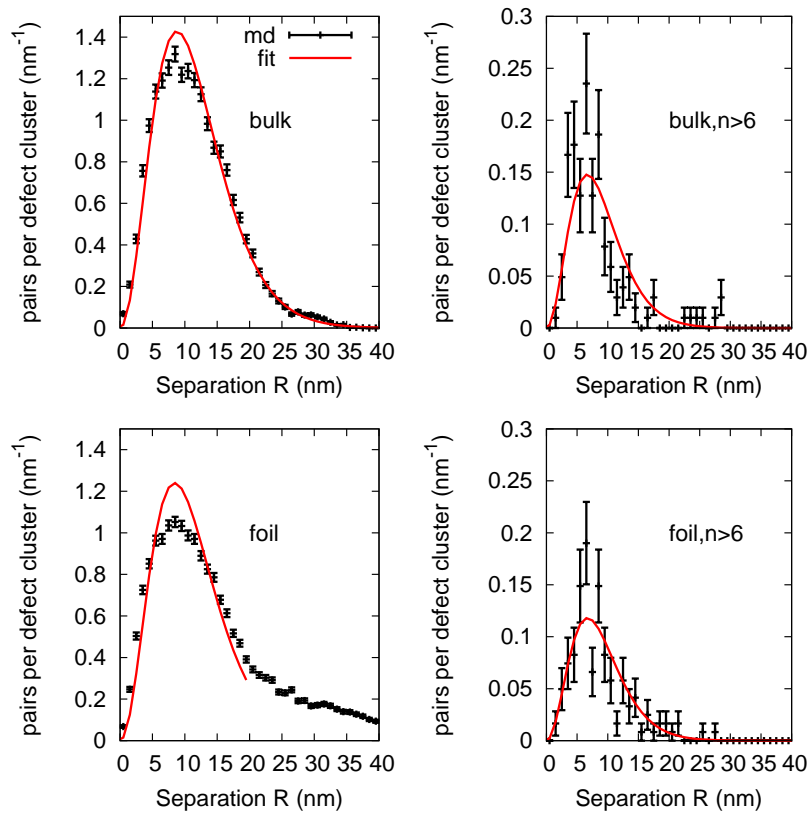


Figure 3: The distribution of defects recorded in MD simulations, together with a single-parameter polynomial-exponential best-fit to the data. The data is shown for all interstitial defects clusters, and for larger clusters ($n > 7$).

assume without proof that the Burgers vectors of loops are independent of their positions, and that one loop moves while the other is fixed.

From Refs [6, 8, 9] we know that the frequency distribution of defect clusters (dislocation loops) containing n point defects is a good fit to a power law, i.e. $f(n) \sim A/n^S$. The probability of a loop size n can therefore be written as $f(n)/Z$ for $1 \leq n \leq n_{max}$ and zero outside. Here Z is the normalization factor for $f(n)$ given by $Z = \sum_{n=1}^{n_{max}} f(n)$. If the initial separation between loops is R , and the angle between the mobile loop normal and the separation is θ , then the distribution of the closest separation for two loops in 3d is

$$\begin{aligned} 4\pi R_0^2 \tilde{P}_{3d}(R_0) &= \frac{1}{4\pi} \int_{\theta=0}^{\pi} \int_{R=0}^{\infty} P_{3d}(R) \delta(|R \sin \theta| - R_0) 4\pi R^2 dR 2\pi \sin \theta d\theta \\ &= \int_{R=R_0}^{\infty} \frac{P_{3d}(R)}{\sqrt{R^2 - R_0^2}} 4\pi R R_0 dR \end{aligned} \quad (9)$$

Following ref [9](supplementary material), we neglect the complex angular dependence of the elastic energy between two loops[28] and instead approximate the elastic energy at this minimum separation as

$$E(R_0) \simeq -\frac{\mu a_0^6}{16\pi(1-\nu)} \frac{n_1 n_2}{R_0^3}, \quad (10)$$

where μ, ν are the shear modulus and Poisson's ratio respectively, a_0 is the lattice parameter, and n_1, n_2 the sizes of the defects. If two loops are generated a depth L below the surface of the foil, and one moves away, it will reach a maximum energy at a depth approximately $L/2$ below the surface before being attracted to its image[9]. The energy barrier to overcome is therefore of order

$$\Delta E \simeq \frac{\mu a_0^6 n_1}{16\pi(1-\nu)} \left(\frac{n_2}{R_0^3} - \frac{7n_1}{8L^3} \right). \quad (11)$$

Therefore if the effective diffusion coefficient for loop movement is D , a loop will still be trapped at time t after generation if[29]

$$\frac{L^2}{4D} \exp\left(\frac{\Delta E}{k_B T}\right) \gtrsim t. \quad (12)$$

This introduces a very simple dynamical evolution into our model. At the time of observation $t > 0$, small or isolated loops will have been lost to the surface. Large loops are more likely to be retained.

However, finding a probability for a defect cluster to be visible in a TEM image from this condition alone is most likely to be an overestimation. No account has yet been taken of the possibility that an interstitial cluster may recombine with vacancies[30]; that pairs of clusters may move in a coordinated fashion[15]; that the incident ion channels straight through the foil[31], or that the cluster is invisible under certain TEM imaging conditions[32] As these loop-loss events should take place whether the defect is elastically trapped or not, we introduce a single tuneable parameter η to account for them all. We therefore write the probability that a defect is trapped by its pair at minimum separation R_0 as

$$\phi(R_0) = \eta \sum_{n_1=1}^{n_{max}} \sum_{n_2=1}^{n_{max}} \frac{f(n_1)f(n_2)}{Z^2} \Theta \left[\Delta E - k_B T \ln \left(\frac{4Dt}{L^2} \right) \right] \tilde{P}_{3d}(R_0). \quad (13)$$

Note that the trapping probability is only logarithmically dependent on both the depth below the surface L , and the time of observation t . The relevant physics is therefore well described assuming that loops are generated below a surface and observed some time after generation. It is also adequate to say that all the loops are generated the same distance L below the surface and observed 60s after generation.

Equation 13 gives the probability that a single pair of loops trap each other. To find the expected number of pairs trapped, \bar{N}_{pair} , we must consider all the possible combinations of trapped and untrapped loops. The calculation of \bar{N}_{pair} is an exercise in graph theory, detailed in appendix Appendix B. The important result is that one visible loop is unlikely to be retained, whereas if multiple loops are generated in a single cascade, they will all be held in place.

The experimental data (figure 4) clearly shows that the apparent density of neighbouring spots tends to zero as $\rho \rightarrow 0$. This is a consequence of the shadowing of spots on the micrograph, namely that loops generated too close together are not resolved individually. We write $\phi_{\text{distinct,intra}}(\rho)$ as the probability that two visible spots are distinct, with $\phi_{\text{distinct,intra}}(\rho \rightarrow 0) = 0$ and $\phi_{\text{distinct,intra}}(\rho \rightarrow \infty) = 1$. A functional form for $\phi_{\text{distinct,intra}}(\rho)$ consistent with the algorithm used to detect spots on the micrograph is developed in appendix Appendix B.

We also see from the experimental data (figure 4) that the apparent density of neighbouring spots tends to a constant value at large ρ . This is the signal from the background of independently generated cascades. However, the apparent dip in the region $\rho \sim 5\text{nm}$ is non-trivial. We believe that this dip has a physical origin in the interaction between cascades: for example, a loop produced independently 5nm away from an existing visible loop can feel an elastic interaction, and so be drawn to it. As an analogue to the intra-cascade overlap, we write $\phi_{\text{distinct,inter}}(\rho)$ as the probability that two cascades will be not overlap, with $\phi_{\text{distinct,inter}}(\rho \rightarrow 0) = 0$ and $\phi_{\text{distinct,inter}}(\rho \rightarrow \infty) = 1$. A functional form for $\phi_{\text{distinct,inter}}(\rho)$ derived from the (fitted) spatial extent of the cascades is developed in appendix Appendix B.

Finally, including the effects of shrinking the cascade as a result of elastic forces acting between the defects and defect clusters, the probability of loop trapping, the overlapping of spots within a cascade and the background of cascades, we arrive at the observed projection of a cascade on the micrograph. Writing the background density of spots on the micrograph as α ,

$$g_{2d}(\rho)d\rho = \left(\bar{N}_{pair} \int_{z=-\infty}^L \phi_{\text{distinct,intra}}(\rho)\phi_{v-v}(R_0) \times \tilde{P}_{3d}(R_0 = \sqrt{\rho^2 + z^2})dz + \alpha\phi_{\text{distinct,inter}}(\rho) \right) 2\pi\rho d\rho. \quad (14)$$

Equation 14 is used to generate a comparison to experiment. Note that while there is a good deal of physics in this expression, the spatial distribution to be fitted is all contained in $P_{3d}(R)$.

3.1. A functional form for intra-subcascade spatial distribution

In principle it is possible to have any form for the intra- cascade spatial distribution function $p(r)$, provided it tends to zero as $r \rightarrow \infty$. With no prior

assumptions, we tried $p(r)$ as a sum of Gaussians. The converged (best) result was for a single Gaussian, with a maximum at $\bar{r} \ll 0$, ie just showing a long tail in the physically meaningful range $r \geq 0$. This leads us to propose the simple exponential form

$$p(r) = \frac{e^{-r/\lambda}}{8\pi\lambda^3}, \quad (15)$$

which we will show leads to good results. Note that we have as yet no theoretical justification for the form of equation 15. Using this we can find an analytical form for $P_{3d}(R)$,

$$P_{3d}(R) = \frac{1}{192\pi\lambda^5} \exp\left(-\frac{R}{\lambda}\right) (R^2 + 3R\lambda + 3\lambda^2). \quad (16)$$

We can also consider the possibility that defect clusters are produced in different subcascades, with a probability x for this to occur. We then need a function $q(r)$ for the probability distribution of the separation between the centres of two subcascades. We have tried a range of polynomial-exponential functions for this, and conclude that $q(r) = r^2 e^{-r/\mu}$ gives best results. The expression for $P_{3d}(R)$, equivalent to equation 6 but for multiple subcascades, is given in appendix Appendix C.

We fit for λ by matching the observed histogram of pairs counted as a function of separation, to a computed histogram. We select the result with the greatest match determined by a chi-squared test.

4. Results

Results for fitting to the MD simulations are shown in figure 3 and table 1. For the bulk MD simulations, we fit to the whole range of separations between defects recorded. For the foil simulations, this proved less effective: An ion penetrating a foil may channel some considerable distance before initiating a cascade, leaving as it does a thin trail of point defects (see figure 1). This trail throws the fitting procedure when all interstitial defect clusters ($n \geq 1$) are taken into account. To mitigate for this effect we fit only to separations recorded up to 20nm. The trail would not be visible in experiment, and it is unclear whether it would be significant for microstructural evolution in self-ion-irradiated tungsten. Taking only larger clusters ($n \geq 7$) into account, we find no evidence of a trail, and a good fit is found for foil simulations.

We find that the total number of defect clusters produced per cascade is similar for bulk and foil MD simulations, about 35, of which 10 having size $n \geq 2$, and 2-4 are larger clusters/loops ($n \geq 7$). We also find that the spatial extent is very similar for bulk and foil. We find $\lambda = 2.2\text{nm}$ for $n \geq 2$ falling to $\lambda = 2.0\text{nm}$ for $n \geq 7$ and further to $\lambda = 1.7\text{nm}$ for $n \geq 13$. This steady decline in apparent cascade size with increasing average loop size suggests that larger loops are more likely to be generated closer to the centre of a cascade.

Results for fitting to the TEM experiments are shown in figure 4 and table 2. There is a minimum observable defect size in a TEM experiment, where

the intensity of the defect becomes undetectable from background noise and, concurrently, the resolution limit of the microscope is reached. It is generally considered that defects of diameter $< 1.5\text{nm}$ can not be seen, and for diameter $< 2\text{nm}$ the count is likely to be low[33] For this work we assume that we see only defects with diameter $> 2\text{nm}$, ($n \geq 55$), whereas in the MD simulations we were taking into account defect clusters containing more than $n \geq 13$. The apparent reduced size of defects in MD is actually just an artefact of the small number of simulations performed[6, 9]. We used a single exponent to fit all the cascade energies, $S = 1.65$ [6, 9]. We find that the fitted total number of defect clusters produced in the 150keV experiments is 32, which compares very well to the MD result (35 defects per cascade), whereas only 0.1 defect clusters per cascade are actually observed.

The characteristic spatial scale of the 150keV cascades observed experimentally is $\lambda = 0.75\text{nm}$, which is considerably smaller than that found for MD ($\lambda = 1.73\text{nm}$ for $n_{vis} = 13$). This smaller size is consistent with the conclusion from the MD simulations that larger loops are generated closer to the centre of a cascade, but at this point we can not claim to have proved that MD simulations give the experimentally observed spatial extent. We observe that all the experimental cascades are similar in spatial extent. This is consistent with the subcascade splitting threshold being around 150keV for self-ions in tungsten, a value of 160keV has been suggested recently based on analysis of BCA cascades [26].

We emphasize that we are not claiming to see loops separated by $\lambda = 0.75\text{nm}$, but rather that the results are most consistent with the tails of a generating distribution with the characteristic size $\lambda = 0.75\text{nm}$. The expected distance from the centre for a single loop generated by an exponential distribution (equation 15) is $\langle r \rangle = \int r p(r) 4\pi r^2 dr = 3\lambda = 2.3\text{nm}$ for 150keV experiment and 5.2 nm in MD. The expected separation between a pair of loops (equation 6) is $\langle R \rangle = \int R P_{3d}(R) 4\pi R^2 dR = 35\lambda/8 = 3.3\text{nm}$ for 150keV experiment and 7.6 nm in MD. An estimate for the expected volume of the cascade can be found from the sphere which has a 50% chance of containing a randomly placed defect cluster, ie the radius r_c where

$$\int_{r=0}^{r_c} p(r) 4\pi r^2 dr = 1/2, \quad (17)$$

which can be solved numerically to give $r_c = 2.674\lambda$. This suggests a containing volume for the MD simulations of $V = 4\pi r_c^3/3 = 410\text{nm}^3$, which can be compared with a recent BCA estimate of the molten heat spike region $V_{BCA} = 580\text{nm}^3$ [26].

5. Discussion and conclusions

In this work we used an algorithm for automating the analysis of black-dot damage as seen in *in situ* TEM ion irradiation experiments. This has enabled us to produce a large, reliable, and above all reproducible dataset of the positions and sizes of the loops observed in ultra-high-purity tungsten foils. We have then pushed the analysis of this dataset to its limits by attempting to find, we believe for the first time, the spatial separation of defects within individual primary damage cascades. This demonstrates that with state-of-the-art electron

	Bulk			
	all	$n \geq 2$	$n \geq 7$	$n \geq 13$
incident ions	28	28	28	28
clusters	1014	324	102	70
pairs recorded	19080	1858	150	70
clusters per cascade \bar{N}	36.2	12.0	3.78	2.59
cascade size λ (nm)	2.63	2.31	1.99	1.8
	Foil			
	all	$n \geq 2$	$n \geq 7$	$n \geq 13$
incident ions	49	49	49	49
ion depth L (nm)	19.0	16.8	14.4	15.8
clusters	1722	493	121	84
pairs recorded	33770	2717	143	66
clusters per cascade \bar{N}	35.14	10.06	2.47	1.71
cascade size λ (nm)	2.52	2.16	2.00	1.73

Table 1: Results for the size of primary cascades measured from MD simulations in the bulk, and in foils.

	Ion energy (keV)			
	50	150	300	400
area (nm ²)	1.71e+07	2.96e+07	1.07E+07	3.05e+07
incident ions	21300	37000	13400	36100
visible defect clusters	2282	4830	1674	8780
visible clusters per cascade	0.134	0.163	0.156	0.288
pairs recorded	8680	20440	6433	63661
ion depth L (nm)	6.9	13.7	24.7	30.6
\bar{N}_{pair}	0.037	0.075	0.057	0.128
efficiency η	0.011	0.0052	0.0041	0.193
clusters per cascade \bar{N}	21.9	32.1	27.4	10.8
cascade size λ (nm)	0.558	0.750	0.560	0.652

Table 2: Results for the size of primary cascades measured from TEM micrographs. The trapping efficiency η and cascade size λ are fitted parameters. Note that the average number of defect clusters \bar{N} is found during the fitting process, and can be directly compared to the total number of defect clusters produced in MD. It is much greater than the average number of visible defect clusters per cascade.

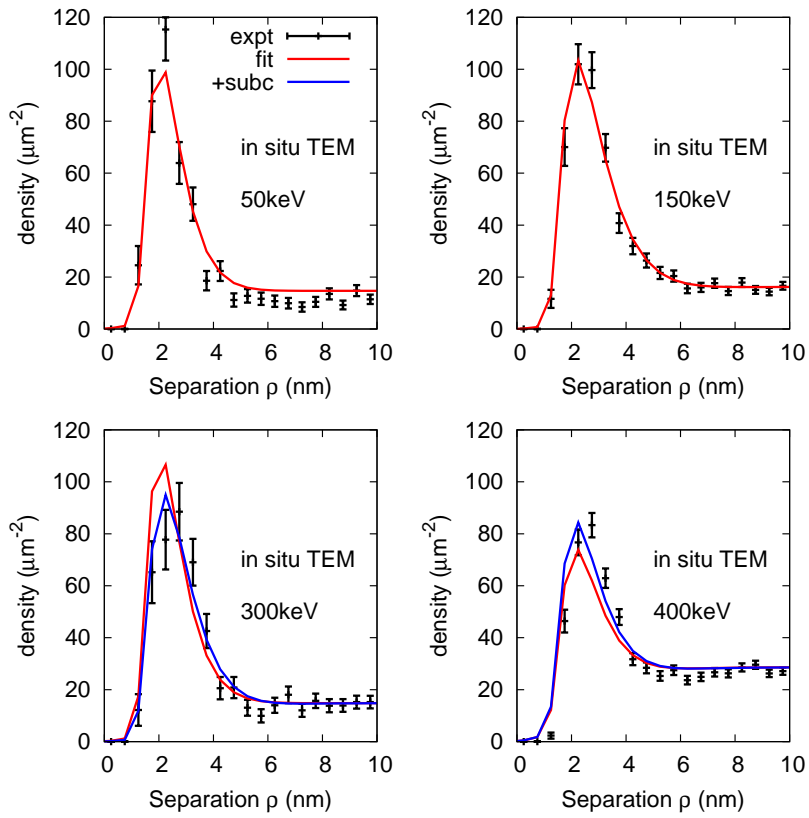


Figure 4: The pair radial distribution function, plotted as the density of loops as a function of distance. The red solid lines show the best fit. The blue solid lines are refitted assuming subcascade branching- these are tighter fits to the data but not significantly so when the additional parameters are taken into account.

microscopy we can discover hidden properties of self-ion-irradiation with a more sophisticated analysis of defect statistics than counting spots alone provided.

We have shown that we can extract the spatial distribution of defect clusters within individual primary damage cascades, and that there is some agreement between MD simulation and experiment. We have also used a simple dynamical argument to find the expected total number of defect clusters produced in a cascade from the smaller number of visible loops in the micrographs. We find excellent agreement between MD and experiment- 35 defect clusters per cascade in MD versus a predicted 32 defect clusters per cascade in the corresponding experiment. This is further evidence that what is seen in the microscope (0.16 defect clusters per cascade) is a tiny fraction of the total damage.

We were able to show that the placement of loops in the micrographs is not random, but is consistent with large loops being randomly placed with a spherically-symmetric radial probability distribution $p(r) \sim \exp(-r/\lambda)$, with $\lambda \sim 1\text{nm}$. Comparison to MD simulations suggest there may be some tendency for larger loops to be more centrally placed; we do not have sufficient data to quantify this effect yet. We have asserted without proof that the loop Burgers vectors are not correlated with their positions, and will explore this effect in the future. We have also not managed to establish the best model for subcascade spatial placement. Experiments performed at much lower fluence might provide a better dataset for this fitting. It would be advantageous also to fit to higher energy MD simulations to find a good functional form for subcascade separation.

Our results provide a second important rationalisation of irradiation damage cascade structure. Our simple form for the spatial extent of cascades can be readily introduced into object kinetic Monte Carlo simulations, and the effect on the subsequent microstructural evolution assessed. It seems clear from the analysis of experimental evidence we have provided here that the cascade size is so small that individual defect clusters strongly interact with each other, and this effect must not be ignored. We have demonstrated methodology to extract and analyse spatial correlations between defects in micrographs which should significantly help future modelling efforts.

6. Acknowledgements

This work has been carried out within the framework of the EUROfusion Consortium and has received funding from the Euratom research and training programme 20142018 under grant agreement No. 633053, and was part-funded by the Research Councils UK Energy Programme [grant number EP/P012450/1]. Grants for computer time from the Center for Scientific Computing in Espoo, Finland, are gratefully acknowledged. The views and opinions expressed herein do not necessarily reflect those of the European Commission.

The experiments of in situ ion irradiations at liquid helium temperature were carried out at Argonne National Laboratory, using the IVEM-Tandem Facility. We thank to Dr Marquis Kirk, Mr Pete Baldo and Edward Eyan for their help with the irradiations. This work was supported by a U.S. Department of Energy Facility funded by the DOE Office of Nuclear Energy, operated under Contract No. DE-AC02-06CH11357 by U. Chicago Argonne, LLC.

The authors would like to thank Jack Haley for helpful discussions and preparing a range of micrographs to test the automated counting procedure.

- [1] H Bolt, V Barabash, G Federici, J Linke, A Loarte, J Roth, and K Sato. Plasma facing and high heat flux materials needs for ITER and beyond. *Journal of Nuclear Materials*, 307311, Part 1:43 – 52, 2002.
- [2] M. Rieth, S.L. Dudarev, and S.M. Gonzalez de Vicente et al. Recent progress in research on tungsten materials for nuclear fusion applications in Europe. *Journal of Nuclear Materials*, 432(13):482 – 500, 2013.
- [3] D.E.J. Armstrong, C.D. Hardie, J.S.K.L. Gibson, A.J. Bushby, P.D. Edmondson, and S.G. Roberts. Small-scale characterisation of irradiated nuclear materials: Part II nanoindentation and micro-cantilever testing of ion irradiated nuclear materials. *Journal of Nuclear Materials*, 462:374 – 381, 2015.
- [4] F. Hofmann, D.R. Mason, J.K. Eliason, A.A. Maznev, K.A. Nelson, and S.L. Dudarev. Non-contact measurement of thermal diffusivity in ion-implanted nuclear materials. *Scientific Reports*, 15:16042, 2015.
- [5] J. Marian, C.S. Becquart, C. Domain, S.L. Dudarev, M.R. Gilbert, R.J. Kurtz, D.R. Mason, K. Nordlund, A.E. Sand, L.L. Snead, T. Suzudo, and Wirth B.D. Recent advances in computational materials modeling of tungsten as plasma-facing material for fusion energy applications. *Nuclear Fusion*, 2016.
- [6] A. E. Sand, S. L. Dudarev, and K. Nordlund. High-energy collision cascades in tungsten: Dislocation loops structure and clustering scaling laws. *EPL (Europhysics Letters)*, 103(4):46003, 2013.
- [7] A.E. Sand, K. Nordlund, and S.L. Dudarev. Radiation damage production in massive cascades initiated by fusion neutrons in tungsten. *Journal of Nuclear Materials*, 455(13):207 – 211, 2014. Proceedings of the 16th International Conference on Fusion Reactor Materials (ICFRM-16).
- [8] X. Yi, A. E. Sand, D. R. Mason, M. A. Kirk, S. G. Roberts, K. Nordlund, and S. L. Dudarev. Direct observation of size scaling and elastic interaction between nano-scale defects in collision cascades. *EPL (Europhysics Letters)*, 110(3):36001, 2015.
- [9] A. E. Sand, D. R. Mason, A. De Backer, X. Yi, S. L. Dudarev, and K. Nordlund. Cascade fragmentation: deviation from power law in primary radiation damage. *Materials Research Letters*, 0(0):1–7, 0.
- [10] D.R. Mason, X. Yi, M.A. Kirk, and S.L. Dudarev. Elastic trapping of dislocation loops in cascades in ion-irradiated tungsten foils. *J. Phys.: Condens. Matter*, 26:375701, 2014.
- [11] Giridhar Nandipati, Wahyu Setyawan, Howard L. Heinisch, Kenneth J. Roche, Richard J. Kurtz, and Brian D. Wirth. Displacement cascades and defect annealing in tungsten, part ii: Object kinetic monte carlo simulation of tungsten cascade aging. *Journal of Nuclear Materials*, 462:338 – 344, 2015.

- [12] C.S. Becquart and C. Domain. An object kinetic monte carlo simulation of the dynamics of helium and point defects in tungsten. *Journal of Nuclear Materials*, 385(2):223 – 227, 2009. Nuclear Materials {IIIProceedings} of the E-MRS 2008 Spring Meeting: Third Symposium N on Nuclear Materials.
- [13] X. Yi, M.L. Jenkins, M. Briceno, S.G. Roberts, Z. Zhou, and M.A. Kirk. In situ study of self-ion irradiation damage in W and W5Re at 500C. *Phil. Mag.*, 93(14):1715–1738, 2013.
- [14] T.D. Swinburne, K. Arakawa, H. Mori, H. Yasuda, M. Isshiki, K. Mimura, M. Uchikoshi, and S.L. Dudarev. Fast, vacancy-free climb of prismatic dislocation loops in BCC metals. *Sci. Rep.*, 6:30596, 2016.
- [15] S. L. Dudarev, M. R. Gilbert, K. Arakawa, H. Mori, Z. Yao, M. L. Jenkins, and P. M. Derlet. Langevin model for real-time Brownian dynamics of interacting nanodefects in irradiated metals. *Phys. Rev. B*, 81:224107, Jun 2010.
- [16] A. Prokhodtseva, B. Décamps, and R. Schäublin. Comparison between bulk and thin foil ion irradiation of ultra high purity Fe. *J Nucl Mater.*, 442:S786–S789, 2013.
- [17] K. Nordlund. PARCAS computer code. The main principles of the molecular dynamics algorithms are presented in Nordlund et al, PRB 57:7556 (1998) and Ghaly et al, Phil Mag A79:795 (1999). the adaptive time step is the same as in nordlund, comp mat sci 3:448 (1995), 2006.
- [18] K. Nordlund, M. Ghaly, R. S. Averback, M. Caturla, T. Diaz de la Rubia, and J. Tarus. Defect production in collision cascades in elemental semiconductors and fcc metals. *Phys. Rev. B*, 57:7556–7570, Apr 1998.
- [19] Mai. Ghaly, Kai. Nordlund, and R. S. Averback. Molecular dynamics investigations of surface damage produced by kiloelectronvolt self-bombardment of solids. *Phil. Mag. A*, 79(4):795–820, 1999.
- [20] K. Nordlund. Molecular dynamics simulation of ion ranges in the 1 100 keV energy range. *Computational Materials Science*, 3(4):448 – 456, 1995.
- [21] H.J.C. Berendsen, J.P.M. Postma, W.F. van Gunsteren, A. DiNola, and J.R. Haak. Molecular dynamics with coupling to an external bath. *J. Chem. Phys.*, 81(8):3684–3690, 1984.
- [22] P. M. Derlet, D. Nguyen-Manh, and S. L. Dudarev. Multiscale modeling of crowdion and vacancy defects in body-centered-cubic transition metals. *Phys. Rev. B*, 76:054107, 2007.
- [23] J.F. Ziegler, J.P. Biersack, and U. Littmark. *The stopping and range of ions in solids*. Pergamon, 1982.
- [24] M. Hou. Fuzzy clustering methods: An application to atomic displacement cascades in solids. *Phys. Rev. A*, 39:2817–2828, Mar 1989.

- [25] Roger E Stoller and Lawrence R Greenwood. Subcascade formation in displacement cascade simulations: Implications for fusion reactor materials. *Journal of Nuclear Materials*, 271272:57 – 62, 1999.
- [26] A. De Backer, A. E. Sand, K. Nordlund, L. Luneville, D. Simeone, and S. L. Dudarev. Subcascade formation and defect cluster size scaling in high-energy collision events in metals. *EPL (Europhysics Letters)*, 115(2):26001, 2016.
- [27] A.I. Ryazanov, E.V. Metelkin, and E.V. Semenov. Modeling of cascade and sub-cascade formation at high {PKA} energies in irradiated fusion structural materials. *Journal of Nuclear Materials*, 386388:132 – 134, 2009. Fusion Reactor Materials Proceedings of the Thirteenth International Conference on Fusion Reactor Materials.
- [28] S.L. Dudarev and A.P. Sutton. Elastic interactions between nano-scale defects in irradiated materials. *Acta Materialia*, 125:425 – 430, 2017.
- [29] B.U. Felderhof. Escape by diffusion from a square well across a square barrier. *Physica A*, 387(1):39–56, 2008.
- [30] T. Jourdan and J.-P. Crocombette. Rate theory cluster dynamics simulations including spatial correlations within displacement cascades. *Phys. Rev. B*, 86:054113, Aug 2012.
- [31] K. Nordlund, F. Djurabekova, and G. Hobler. Large fraction of crystal directions leads to ion channeling. *Phys. Rev. B*, 94:214109, Dec 2016.
- [32] Z. Zhou, M. L. Jenkins, S. L. Dudarev, A. P. Sutton, and M. A. Kirk. Simulations of weak-beam diffraction contrast images of dislocation loops by the many-beam Howie-Basinski equations. *Philosophical Magazine*, 86(29-31):4851–4881, 2006.
- [33] C. Liu, L. He, Y. Zhai, B. Tyburska-Pschel, P.M. Voyles, K. Sridharan, D. Morgan, and I. Szlufarska. Evolution of small defect clusters in ion-irradiated 3C-SiC: Combined cluster dynamics modeling and experimental study. *Acta Materialia*, 125:377 – 389, 2017.
- [34] R. Fischer, K. M. Hanson, V. Dose, and W. von der Linden. Background estimation in experimental spectra. *Phys. Rev. E*, 61:1152–1160, Feb 2000.
- [35] A. Lindeberg. *Scale-Space Theory in Computer Vision*. Springer Science+Business Media Dordrecht, 1994.
- [36] T.W. Ridler and S. Calvard. Picture thresholding using an iterative selection method. *IEEE TRANSACTIONS ON SYSTEMS, MAN, AND CYBERNETICS*, SMC-8:630–632, 1978.
- [37] J.A. Högbom. Aperture synthesis with a non-regular distribution of interferometer baselines. *Astron. Astrophys. Suppl.*, 15:417–426, 1974.
- [38] Marquis Kirk, Xiaou Yi, and Michael Jenkins. Characterization of irradiation defect structures and densities by transmission electron microscopy. *Journal of Materials Research*, 30(9):11951201, 2015.

Appendix A. Automated micrograph analysis

A common issue with TEM micrographs is the variation in intensity of the background due to foil thickness changes or foil bends. These variations are easy to spot by eye as their wavelength is typically somewhat longer than the features of interest, but they present a big problem for automated analysis- bright background may be counted as a feature, or a dim spot on a dark background may be ignored as its intensity falls below an arbitrary threshold. Most algorithms must start by removing background, but this is difficult to do without altering the shape of the feature to be detected.

Our algorithm for background removal works by estimating pixel-by-pixel both the average background intensity, and the probability that it should be treated as background. This dual approach has previously been demonstrated by Fischer et al[34]; our approach is simpler, and closer in feel to blob detection in computer vision[35].

We start by convolving the image intensity $f(x, y)$ with a Gaussian kernel of width t (to blur):

$$g(x, y; t) = \exp\left(-\frac{x^2 + y^2}{2t^2}\right) \quad (\text{A.1})$$

and a logistic function centred on an assumed background level b with spread s (to separate foreground):

$$h(x, y; b, s) = \frac{1}{1 + \exp\left(\frac{f(x, y) - b}{s}\right)}. \quad (\text{A.2})$$

Note that as defined $h \rightarrow 1$ for low-intensity (background) pixels. To work with dark features on a bright background, we simply start with the negative of the image. The convolution gives a representation of the background in scale-space ¹

$$L(x, y; t) = \frac{\sum_{x', y'} f(x', y') h(x', y'; b, s) g(x' - x, y' - y; t)}{\sum_{x', y'} h(x', y'; b, s) g(x' - x, y' - y; t)} \quad (\text{A.3})$$

The magnitude of the gradient $|\partial L / \partial t|$ is an indication of how fast the image intensity is varying at length-scale t . We then make the following assumption: For a pixel in the background, the characteristic length-scale is long, but we can use the background average of a very local region. Conversely, for a pixel in the foreground the characteristic length-scale is short, and we should use the background averaged over a wide region. To find a good background estimate we therefore need to reverse length-scales. We compute a new estimate of the background pivoting on a feature length-scale t_0 with

$$\tilde{f}(x, y) = \frac{\int_{t=0}^{2t_0} \left| \frac{\partial L}{\partial t} \right| L(x, y; 2t_0 - t) dt}{\int_{t=0}^{2t_0} \left| \frac{\partial L}{\partial t} \right| dt}. \quad (\text{A.4})$$

and then mix this with the image to find a new background

$$f'_0(x, y) = \xi h(x, y; b, s) f(x, y) + (1 - \xi h(x, y; b, s)) \tilde{f}(x, y). \quad (\text{A.5})$$

¹In the following treatment we assume dead pixels, foil edges, edge dislocation lines, oxide particles and other obvious regions not to be counted are excluded from summations.



Figure A.5: TEM image background removal. Bright-field image of Fe-9Cr irradiated to 1.8dpa at 350C. Left: original image with varying background. Centre: computed background signal. Right: image with background subtracted. Image courtesy Jack Haley, Oxford University.

We use a mixing parameter $\xi = 1/2$ for numerical stability.

To initialise the logistic function, we set b to be the average intensity of the background pixels below the Ridler & Calvard threshold[36], and σ their standard deviation. We then note that were the image intensity standard deviation is σ , with average b then using Sommerfeld's expansion we should find the average under convolution with the logistic function alone would be

$$\bar{f} = \frac{\sum_{x,y} f(x,y) h(x,y;b,s)}{\sum_{x,y} h(x,y;b,s)} = b - \sqrt{2}\pi\sigma + \sqrt{\frac{\pi^2}{2}} \frac{s^2}{3\sigma} - \dots, \quad (\text{A.6})$$

and so if we set $s = \sqrt{6}\sigma/\pi$, then $\bar{f} = b$, we therefore preserve the average intensity level.

Our algorithm for background removal is then

1. seed the logistic function using the Ridler & Calvard threshold
2. compute a revised estimate for the background level with equation A.5
3. compute the new image with

$$f'(x,y) = f(x,y) - f'_0(x,y) + b_0, \quad (\text{A.7})$$

where b_0 is the desired background level.

This process is iterated until convergence. An illustration is given in figure A.5.

The second half of the task of automated image analysis is to identify the features. In this case we are looking for dislocation loops, which in weak-beam dark-field imaging appear as white blobs on a dark background. At low fluence, rings and coffee-bean shaped features are rare, so we can map the features to 2d Gaussians. This is a well-known problem in computer vision, but existing astronomy literature solutions (eg variants of the CLEAN algorithm[37]) perform poorly with TEM images, where the overlaps can be large and multiple maxima should be ascribed to the same feature.

A 2d Gaussian is defined by a centre (x,y) , major- and minor- axes radii (s_1, s_2) , an angle θ , and intensity I : 5 parameters in all. We seek to minimise an objective function S , using n_G 2d Gaussians

$$S = \sum_{x,y} \left(f(x,y) - b_0 - \sum_{i=1}^{n_G} g(x_i, y_i, s_{1i}, s_{2i}, I_i) \right)^2, \quad (\text{A.8})$$

which is a straightforward minimisation problem as first derivatives are available, provided a good initial guess can be found.

To find the best sum of 2d Gaussians, our procedure is:

1. Find a region of interest (ROI) in the image. A ROI is defined as a contiguous region of pixels where $f(x, y) - b_0 > 2\sigma$, where b_0 is the average background level and σ the background standard deviation. Crop this region for further investigation.
2. Compute the t-test statistic $t = \frac{\bar{f} - b_0}{\sigma/\sqrt{n}}$ for the ROI, where \bar{f} is the average intensity in the ROI, and n the number of pixels. Reject the ROI if $t < 6.3$, which is equivalent to rejecting the region if there is a greater than 5% chance it is a result of random fluctuation.
3. Perform a blur with a 1/2 pixel Gaussian kernel to reduce spurious shot noise in the ROI.
4. Find local maxima- those pixels whose 4 nearest neighbours are all of lower intensity. Index the pixels containing these maxima, leave other pixels unassigned. Combine maxima within 2 pixels range.
5. For each unassigned pixel, index to same maximum as the highest intensity assigned neighbour. Repeat until every pixel is assigned to one maximum.
6. Now consider the valleys between maxima. If there exists a pixel on an interface between two maxima whose intensity does not drop below $d = 90\%$ of the linearly interpolated intensity between the maxima, there must be a bright path between these two maxima. Combine these two maxima. Repeat until pixel is assigned to one region.
7. For each region a , relax a single 2d Gaussian by optimising equation A.8 within its assigned pixels. Compute $w_a = \sum_{x,y \in a} (f(x, y) - b_0)^2$ and rank each region by weight. This step completes the initial guess.
8. Take the regions with the n_G highest weights, and using the Gaussians from the previous step as an initial condition, relax by optimising equation A.8 over the whole ROI.
9. Select the best fit as the sum of Gaussians which produces the minimum value $n_G S$.
10. Reject those Gaussians for which the eccentricity $e = s_1/s_2 > 2.5$.

Our solution detects two-thirds of the spots if ten simulated spots are superimposed into a 30x30px square, with position and width errors of 2 and 0.5 pixels respectively. For isolated spots we have near perfect reconstruction of simulated images. An illustration of this procedure with simulated data is given in figure A.6.

To complete the automated analysis we must define a loop image radius from the 2d Gaussian. This we have done by matching the size of thousands of individual loops determined by our automated method to the size using the standard methodology of Kirk et al[38]. We recommend reporting the loop image radius as $2s_1$, ie twice the Gaussian standard deviation in the major axis direction. We would also recommend that the intensity level for maxima to be combined (d) and maximum permitted eccentricity (e) be tuned for best results. An illustration is given in figure A.7.

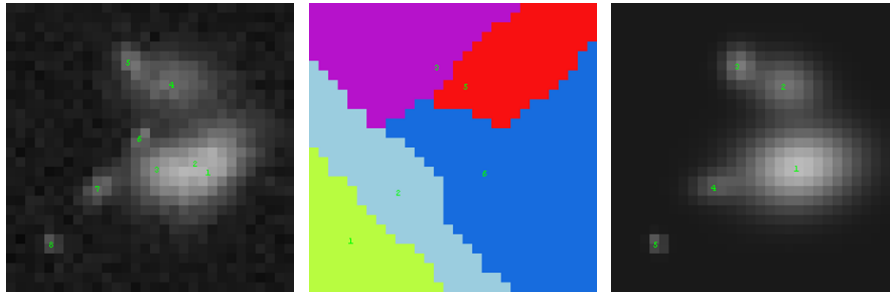


Figure A.6: Fitting 2D Gaussians to noisy images. Left- 8 computer generated overlapping peaks. Middle- analysing the watersheds and combining maxima leaves five potential regions. Right- computer interpretation of five 2d Gaussian peaks. The algorithm finds good positions and spot sizes, but will unavoidably lose a few peaks in a noisy image.

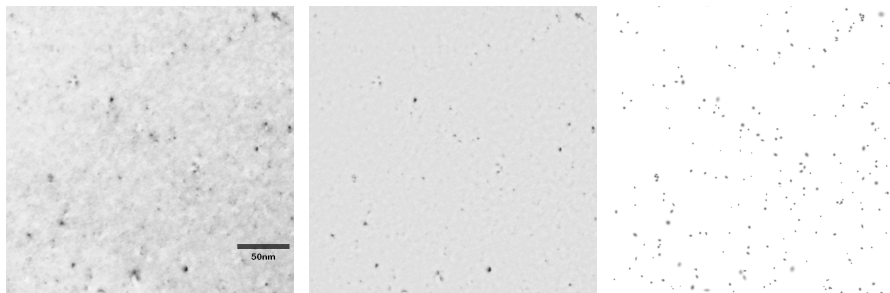


Figure A.7: Automatic analysis of loops. 150keV W+ in UHP W @ 30K, WBDF TEM (shown in negative to emphasize the background variation). Left: received TEM image. Centre: background subtracted image. Right: analysed image.

Appendix B. Probability of elastic trapping, and of intra- and inter-cascade overlap

Equation 13 gives the probability that a single pair is trapping. We can integrate to find the trapping probability per pair is $\phi = \int \phi(R_0) 4\pi R_0^2 dR_0$. We can find the conditional probability that a pair is trapped given that it is between a visible loop and an invisible cluster (ϕ_{v-i}), or between two visible loops (ϕ_{v-v}), by changing the ranges of the summations (and normalisation) in equation 13.

To find the number of visible loops trapped, and hence the number of visible pairs we must go further: at some percolation threshold all loops will be trapped. If there is a small number N_v visible loops, and a small number N_i invisible clusters, it is a simple matter to evaluate all possible graphs² and compute the probability for the number of visible, trapped loops explicitly. If $N_v + N_i \gtrsim 8$, the number of graphs becomes prohibitive. But we can find a good approximation to the probability of the number of loops as follows: If the loops are generated independently, the probability distribution for the number of visible loops will be binomially distributed. We then approximate the probability distributions for the number of visible-invisible trapping bonds (n_{v-i}) and for the number of visible-visible trapping bonds (n_{v-v}) as binomially distributed and independent (see figure B.8). Then the probability of N_{vt} visible, trapped loops given N total defects produced is approximated by the heuristic

$$\begin{aligned}
 p(N_{vt} | \phi_{v-v}, \phi_{v-i}, N) &\sim \sum_{N_v=0}^N \sum_{n_{v-v}=0}^{N_{vt}(N_{vt}-1)/2} \sum_{n_{v-i}=0}^{N_{vt}N_i} \binom{N}{N_v} \binom{N_v}{N_{vt}} p_v^{N_v} (1-p_v)^{N-N_v} \\
 &\times \binom{N_{vt}(N_{vt}-1)/2}{n_{v-v}} \phi_{v-v}^{n_{v-v}} (1-\phi_{v-v})^{N_v(N_v-1)/2-n_{v-v}} \\
 &\times \binom{N_{vt}N_i}{n_{v-i}} \phi_{v-i}^{n_{v-i}} (1-\phi_{v-i})^{N_vN_i-n_{v-i}} \quad (\text{B.1})
 \end{aligned}$$

Note that this expression needs normalising to ensure $\sum_{N_{vt}=0}^N p(N_{vt} | \phi_{v-v}, \phi_{v-i}, N) = 1$.

We use explicit summations over graphs for $N_v + N_i \leq 8$ and equation B.1 for $N_v + N_i > 8$. In practice we have found it expedient to tabulate and store $p(N_v | \phi_{v-v}, \phi_{v-i}, N)$ at a range of values for $(\phi_{v-v}, \phi_{v-i}, N)$ and interpolate. If we assume that the defects are produced independently, then the total number of defects produced per cascade, N , is Poisson distributed. We can then compute the number of observable spots, and visible pairs, per incident ion:

$$\bar{N}_{vt} = \sum_N \sum_{N_{vt}} N_{vt} p(N_{vt} | \phi_{v-v}, \phi_{v-i}, N) P_{\text{Poisson}}(N | \bar{N}) \quad (\text{B.2})$$

$$\bar{N}_{pair} = \sum_N \sum_{N_{vt}} \frac{N_{vt}(N_{vt}-1)}{2} p(N_v | \phi_{v-v}, \phi_{v-i}, N) P_{\text{Poisson}}(N | \bar{N}). \quad (\text{B.3})$$

²There are $N_v(N_v-1)/2 + N_vN_i$ pairs which might trap visible loops to consider, and so counting pairs as trapping or not, there are two to the power of this number of graphs. We need to draw each graph and count the number of visible defects with at least one trapping pair.

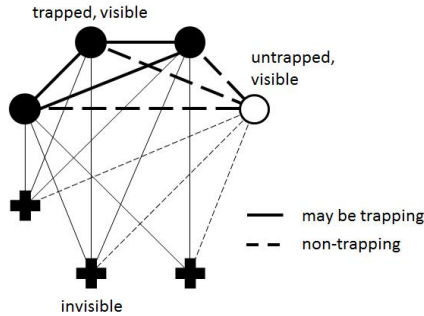


Figure B.8: A sketch to illustrate finding the probability of N_{vt} trapped, visible loops. $N_v = 4$ circles represent loops large enough to be visible, of which $N_{vt} = 3$ filled circles are trapped. $N_i = 3$ crosses are loops too small to be visible. Bold lines between visible loops have a probability ϕ_{v-v} of being trapping, faint lines have probability ϕ_{v-i} of being trapping. We must find all combinations of $N_{vt}(N_{vt} - 1)/2$ visible-visible traps, together with all $N_{vt}N_i$ visible-invisible traps, counting only those graphs where N_{vt} visible loops have one or more trapping pairs. This can be done explicitly for $N_v + N_i \leq 8$, and approximately using equation B.1 for larger numbers.

\bar{N}_{vt} is determined directly from the micrograph- it is the number of visible spots divided by the number of incident ions. We find \bar{N} by numerically inverting equation B.2. Equation B.3 then gives the number of pairs expected to be recorded on the micrograph per incident ion.

We now consider the number of spots in a 2d image which can not be resolved because they appear to overlap. Assume that a spot is formed by a circular dislocation loop containing n point defects with Burgers vector b , and characteristic radius $\rho(n) = \sqrt{\frac{\Omega n}{\pi b}}$, where Ω is the volume per atom. Two spots may be resolved when their separation $R > \zeta(\rho(n_1) + \rho(n_2))$, with ζ a small numerical constant. Now ζ is difficult to compute generally, as it is dependent on the shape of the spot in the imaging conditions and the algorithm used to extract spots. Furthermore, the number of spots recorded at small R is sensitive to the choice of ζ . We estimate $\zeta = 0.63$ as follows: Consider two equal height Gaussians of width σ separated by R . They are resolved by the automatic counting procedure if their sum midway between the two is less than 90% of the peak height, ie $2 \exp(-(R/2)^2/2\sigma^2) < 0.9$ (see appendix Appendix A). We interpret the radii of spots on the micrograph as $\rho \sim 2\sigma$. Hence we need $R > \sqrt{\ln \sqrt{2/0.9}}(\rho(n_1) + \rho(n_2)) \approx 0.63(\rho(n_1) + \rho(n_2))$.

We can therefore find the fraction of loops which overlap as a function of separation

$$\phi_{\text{distinct,intra}}(R) = 1 - \sum_{n_1=n_{vis}}^{n_{max}} \sum_{n_2=n_{vis}}^{n_{max}} \frac{f(n_1)f(n_2)}{Z_{vis}^2} \Theta [\zeta(\rho(n_1) + \rho(n_2)) - R], \quad (\text{B.4})$$

where $\Theta(x)$ is the Heaviside function.

Finally consider the background of cascades. If a second cascade appears too close to the first, it will be indistinguishable. Alternatively if it is initiated close to the first, it may interact strongly and appear to be absorbed. A full

analysis of the dynamics of interacting primary damage cascades is beyond the scope of this paper, and indeed it is difficult to disentangle overlap effects from snapshots of the irradiation, but we can produce a good estimate for the fraction of the overlap from the spatial extent. This is then used to find the density of spots in the background which can be deemed distinct. We write the degree of overlap for two cascades separated by ρ in the micrograph image as

$$\phi_{\text{distinct,inter}}(\rho) = 1 - \frac{\int P_{2d,\text{casc}}\left(\sqrt{(x-\rho/2)^2+y^2}\right) P_{2d,\text{casc}}\left(\sqrt{(x+\rho/2)^2+y^2}\right) dx dy}{\int P_{2d,\text{casc}}(\rho') P_{2d,\text{casc}}(\rho') 2\pi\rho' d\rho'}. \quad (\text{B.5})$$

Appendix C. Analytical forms for spatial distribution with subcascades

In this appendix we present the analytical forms for the distance between two defects and their closest approach. We start with the polynomial-exponential forms for intra- and inter- subcascade spatial distributions.

$$p_1(r) = \frac{e^{-r/\lambda}}{8\pi\lambda^3}, \quad (\text{A.1})$$

and

$$q(r) = \frac{r^2 e^{-r/\mu}}{96\pi\mu^5}, \quad (\text{A.2})$$

where we interpret $q(r)$ as the probability distribution for the distance between the centres of subcascades. We have also tried $q(r) \sim e^{-r/\mu}$ and $q(r) \sim r e^{-r/\mu}$, and concluded that equation A.2 is the best form.

Using this we can find the spatial distribution for a defect in a second subcascade relative to the origin of the first subcascade. We note that this is exactly the same integral as equation 6, and write

$$\begin{aligned} q_2(r) &= \frac{2\pi}{r} \int_{r_1=0}^{\infty} \int_{r_2=|r-r_1|}^{r+r_1} p_1(r_1) q(r_2) r_1 r_2 dr_1 dr_2 \\ &= \frac{\lambda^3 e^{-r/\lambda}}{8\pi r (\lambda^2 - \mu^2)^5} \left\{ r(\lambda^4 - \mu^4) - 10\lambda^3 \mu^2 - 6\lambda \mu^4 \right\} \\ &+ \frac{e^{-r/\mu}}{96\pi r \mu (\lambda^2 - \mu^2)^5} \left\{ \begin{aligned} &(r^3(\lambda^2 - \mu^2)^3 + 12r^2 \mu \lambda^2 (\lambda^2 - \mu^2)^2 \\ &+ 12r(5\lambda^6 \mu^2 - 4\lambda^4 \mu^4 - \lambda^2 \mu^6) + 24\lambda^4 \mu^3 (5\lambda^2 + 3\mu^2) \end{aligned} \right\}. \end{aligned} \quad (\text{A.3})$$

So, if the probability that the second defect cluster is in a second subcascade is x , we can then write the spatial distribution for the second defect cluster as a function of the distance from the origin of the subcascade containing the *first* defect cluster, $p_2(r) = (1-x)p_1(r) + xq_2(r)$. The probability distribution for

the distance between two defects is then found by employing equation 6 again:

$$\begin{aligned}
P_{3d}(R) &= \frac{2\pi}{R} \int_{r_1=0}^{\infty} \int_{r_2=|R-r_1|}^{R+r_1} p_1(r_1)p_2(r_2) r_1 r_2 dr_1 dr_2. \\
&= \frac{e^{-R/\lambda}}{192\pi\lambda^5} \{R^2 + 3R\lambda + 3\lambda^2\} \\
&+ \frac{x\mu^3 e^{-R/\mu}}{96\pi R(\lambda^2 - \mu^2)^7} \left\{ \begin{array}{l} R^3(\lambda^2 - \mu^2)^3 \\ +24R^2\lambda^2\mu(\lambda^2 - \mu^2)^2 \\ +24R\lambda^2\mu^2(\lambda^2 - \mu^2)(9\lambda^2 + \mu^2) \\ +240\lambda^4\mu^3(3\lambda^2 + \mu^2) \end{array} \right\} \\
&+ \frac{x\mu^2 e^{-R/\lambda}}{192\pi R\lambda^5(\lambda^2 - \mu^2)^7} \left\{ \begin{array}{l} 5R\lambda^{12}(R^2 - 3R\lambda - 3\lambda^2) \\ -21R\lambda^{10}\mu^2(R^2 + R\lambda - 15\lambda^2) \\ +\lambda^8\mu^4(37R^3 + 117R^2\lambda - 75R\lambda^2 - 1440\lambda^3) \\ -6\lambda^6\mu^6(6R^3 + 21R^2\lambda + 45R\lambda^2 + 80\lambda^3) \\ +21R\lambda^4\mu^8(R^2 + 3R\lambda + 3\lambda^2) \\ -7R\lambda^2\mu^{10}(R^2 + 3R\lambda + 3\lambda^2) \\ +R\mu^{12}(R^2 + 3R\lambda + 3\lambda^2) \end{array} \right\}. \tag{A.4}
\end{aligned}$$

This expression is analytic in its limits

$$\lim_{R \rightarrow 0} P_{3d}(R) = \frac{1 + x \left(\frac{\lambda^5(\lambda^2 + 7\lambda\mu + 16\mu^2)}{(\lambda + \mu)^7} - 1 \right)}{64\pi\lambda^3}, \tag{A.5}$$

$$\begin{aligned}
\lim_{\mu \rightarrow \lambda} P_{3d}(R) &= \frac{e^{-R/\lambda}}{192\pi\lambda^5} \{R^2 + 3R\lambda + 3\lambda^2\} \\
&+ \frac{x e^{-R/\lambda}}{1290240\pi\lambda^9} \left\{ \begin{array}{l} R^6 + 14R^5\lambda + 105R^4\lambda^2 + 525R^3\lambda^3 \\ -4935R^2\lambda^4 - 16380R\lambda^5 - 16380\lambda^6 \end{array} \right\}. \tag{A.6}
\end{aligned}$$